

PEPNET: A LIGHTWEIGHT POINT-BASED EVENT CAMERA 6-DOFs POSE RELOCALIZATION NETWORK

Anonymous authors

Paper under double-blind review

ABSTRACT

1 Event cameras exhibit remarkable attributes such as high dynamic range, asyn-
2 chronicity, and low latency, making them highly suitable for vision tasks that in-
3 volve high-speed motion in challenging lighting conditions. These cameras im-
4 plicitly capture movement and depth information in events, making them appeal-
5 ing sensors for Camera Pose Relocalization (CPR) tasks. Nevertheless, existing
6 CPR networks based on events neglect the pivotal fine-grained temporal infor-
7 mation in events, resulting in unsatisfactory performance. Moreover, the energy-
8 efficient features are further compromised by the use of excessively complex mod-
9 els, hindering efficient deployment on edge devices. In this paper, we introduce
10 PEPNet, a lightweight point-based network designed to regress six degrees of free-
11 dom (6-DOFs) event camera poses. We rethink the relationship between the event
12 camera and CPR tasks, leveraging the raw point cloud directly as network input
13 to harness the high-temporal resolution and inherent sparsity of events. PEPNet
14 is adept at abstracting the spatial and implicit temporal features through hierar-
15 chical structure and explicit temporal features by Attentive Bi-directional Long
16 Short-Term Memory (A-Bi-LSTM). By employing a carefully crafted lightweight
17 design, PEPNet delivers state-of-the-art (SOTA) performance on public datasets
18 with meager computational resources. Specifically, PEPNet attains a significant
19 38% performance improvement on the random split DAVIS 240C CPR Dataset,
20 utilizing merely 6% of the parameters compared to traditional frame-based ap-
21 proaches. Moreover, the lightweight design version PEPNet_{tiny} accomplishes
22 results comparable to the SOTA while employing a mere 0.5% of the parameters.

23 1 INTRODUCTION

24 Event cameras are a type of bio-inspired vision sensor that responds to local changes in illumination
25 that exceed a predefined threshold (Lichtsteiner et al., 2008). Differing from conventional frame-
26 based cameras, event cameras independently and asynchronously emit pixel-level events. Notably,
27 event cameras boast an exceptional triad: high dynamic range, low latency, and ultra-high temporal
28 resolution. This unique combination empowers superior performance under challenging light condi-
29 tions, adeptly capturing the swift scene and rapid motion changes in near-microsecond precision
30 (Posch et al., 2010). Additionally, event cameras boast remarkably low power consumption. Due
31 to their inherent hardware attributes, event cameras have garnered significant attention in the fields
32 of computer vision and robotics in recent years, positioning them as a popular choice for many
33 power-constrained devices like wearable devices, mobile drones, and robots (Delbruck & Lang,
34 2013; Gallego et al., 2020; Mitrokhin et al., 2019). Camera Pose Relocalization (CPR) is such an
35 example. CPR facilitates the accurate estimation of a camera’s pose within the world coordinate
36 system (Sünderhauf et al., 2015). It is extensively employed in numerous applications, including
37 Virtual Reality (VR), Augmented Reality (AR), and robotics (Shavit & Ferens, 2019).

38 CPR tasks using event cameras significantly diverge from their conventional CPR counterpart that
39 employs frame-based cameras, primarily due to the inherent dissimilarity in data output mecha-
40 nisms between these two camera types. Furthermore, events inherently encompass information
41 regarding object motion and depth changes across precise temporal and spatial dimensions at-
42 tributes of paramount significance within the domain of CPR tasks (Rebecq et al., 2018; Gallego

et al., 2017). Regrettably, existing event-based CPR networks often derive from the conventional camera network paradigms and inadequately address the unique attributes of event data. More specifically, events are transformed into various representations such as event images (Nguyen et al., 2019), time surfaces (Lin et al., 2022), and other representations (Lin et al., 2022), leading to the loss of their fine-grained temporal information. Furthermore, most event-based methods tend to overlook the computational load of the network, only prioritizing elevated accuracy, which contradicts the fundamental design principles of event cameras (Gallego et al., 2020).

Point Cloud is a collection of 3D points (x, y, z) that represents the shape and surface of an object or environment and is often used in lidar and depth cameras (Guo et al., 2020). Event Cloud is a collection of events (x, y, t, p) generated by event cameras, t represents timestamps and p is the polarity. By treating each event’s temporal information as the third dimension, event inputs (x, y, t) can be transformed into points and aggregated into a pseudo-Point Cloud (Wang et al., 2019; Qi et al., 2017a;b). However, a direct transplantation of the Point Cloud network has not yet exhibited an amazing performance advantage in processing event data. Given that the t dimension of Event Cloud is not strictly equivalent to the spatial dimensions (x, y, z) , customizing the Point Cloud network becomes imperative to adequately capture the temporal information of events.

In this study, we introduce PEPNet, an innovative end-to-end CPR network designed to harness the attributes of event cameras. A comparison of our method to other event-based methods is illustrated Figure 2 in in red and blue, respectively. Our main contributions are as follows: First, PEPNet directly processes the raw data obtained from the event cameras, meticulously preserving the fine-grained temporal information and the order inherent in the data. Second, PEPNet proficiently captures spatial features and implicit temporal patterns through its hierarchical structure with temporal aggregation. Additionally, it effectively incorporates explicit temporal features using A-Bi-LSTM. This architecture is tailored to accommodate the high temporal resolution and sparse characteristics inherent in event cameras. Third, PEPNet not only attains SOTA results on a public dataset (Mueggler et al., 2017) but also can be executed in real-time with a lightweight design as shown in Figure 1. Diverging from other point-based approaches in event data processing (Wang et al., 2019; Ren et al., 2023), PEPNet stands out by meticulously considering the distinction between Event Cloud and Point Cloud in its design. This thoughtful approach enables the precise extraction of spatio-temporal features and facilitates solutions for a spectrum of event-based tasks.

2 RELATED WORK

2.1 FRAME-BASED CPR LEARNING METHODS

Deep learning, crucial for vision tasks like classification and object detection (LeCun et al., 2015), has seen advancements such as PoseNet’s innovative transfer learning (Kendall et al., 2015). Utilizing VGG, ResNet (Simonyan & Zisserman, 2014; He et al., 2016), LSTM, and customized loss functions (Walch et al., 2017; Wu et al., 2017; Naseer & Burgard, 2017), researchers enhanced this approach. Auxiliary Learning methods further improved performance (Valada et al., 2018; Radwan et al., 2018; Lin et al., 2019), although overfitting remains a challenge. Hybrid pose-based methods, combining learning with traditional pipelines (Laskar et al., 2017; Balntas et al., 2018), offer promise. DSAC series, for instance, achieve high pose estimation accuracy (Brachmann & Rother, 2021; Brachmann et al., 2017), but come with increased computational costs and latency, especially for edge devices.

2.2 EVENT-BASED CPR LEARNING METHODS

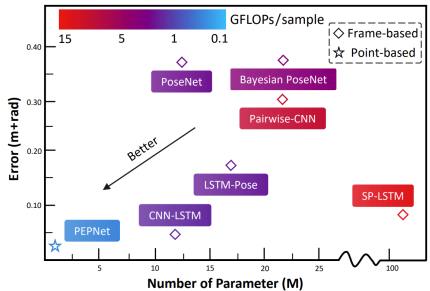


Figure 1: The average results using the random split method benchmarked on the CPR dataset (Mueggler et al., 2017). The vertical axis represents the combined rotational and translational errors (m+rad). PEPNet is the first point-based CPR network for event cameras.

95 Event-based CPR methods often derive from
 96 the frame-based CPR network. SP-LSTM
 97 (Nguyen et al., 2019) employed the stacked
 98 spatial LSTM networks to process event im-
 99 ages, facilitating a real-time pose estimator. To
 100 address the inherent noise in event images, (Jin
 101 et al., 2021) proposed a network structure com-
 102 bining denoise networks, convolutional neural
 103 networks, and LSTM, achieving good perfor-
 104 mance under complex working conditions. In
 105 contrast to the aforementioned methods, a novel
 106 representation named Reversed Window Entropy
 107 Image (RWEI) (Lin et al., 2022) is intro-
 108 duced, which is based on the widely used event
 109 surface (Mitrokhin et al., 2020) and serves as
 110 the input to an attention-based DSAC* pipeline (Brachmann & Rother, 2021) to achieve SOTA
 111 results. However, the computationally demanding architecture involving representation transfor-
 112 mation and hybrid pipeline poses challenges for real-time execution. Additionally, all existing methods
 113 ignore the fine-grained temporal feature of the event cameras, and accumulate events into frames for
 114 processing, resulting in unsatisfactory performance.

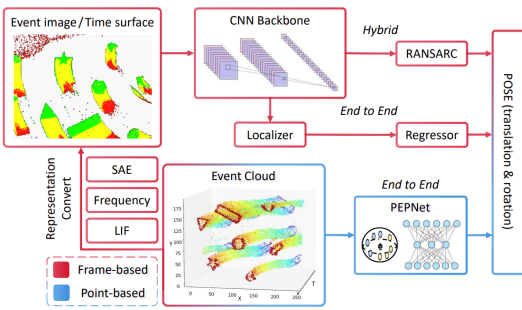


Figure 2: Two different event-based processing methods, frame-based and point-based.

115 2.3 POINT CLOUD NETWORK

116 Point-based methodologies have transformed the direct processing of Point Cloud, with PointNet (Qi
 117 et al., 2017a) as a standout example. Taking a step beyond, PointNet++ (Qi et al., 2017b) introduced
 118 a Set Abstraction module. While it initially employed a straightforward MLP in the feature extractor,
 119 recent advancements have seen the development of more sophisticated feature extractors to enhance
 120 Point Cloud processing (Wu et al., 2019; Zhao et al., 2021; Ma et al., 2021; Dosovitskiy et al.,
 121 2020). When extending these techniques to Event Cloud, Wang et al. (Wang et al., 2019) were
 122 the first to address the temporal information processing challenge while maintaining representation
 123 in both the x and y axes, enabling gesture recognition using PointNet++. Further enhancements
 124 came with PAT (Yang et al., 2019), which incorporated self-attention and Gumbel subset sampling,
 125 leading to improved performance in recognition tasks. However, existing point-based models still
 126 fall short in performance compared to frame-based methods. This phenomenon can be attributed to
 127 the distinctively different characteristics of Point Cloud and Event Cloud. Event Cloud contradicts
 128 the permutation and transformation invariance present in Point Cloud due to its temporal nature.
 129 Additionally, the Point Cloud network is not equipped to extract explicit temporal features.

130 3 PEPNET

131 PEPNet pipeline consists of four essential modules: (1) a preprocessing module for the origi-
 132 nal Event Cloud, (2) a hierarchical point cloud feature extraction structure, (3) an Attentive Bi-
 133 directional LSTM, and (4) a 6-DOFs pose regressor, as illustrated in Figure 3. In the following
 134 sections, we will provide detailed descriptions and formulations for each module.

135 3.1 EVENT CLOUD

136 To preserve the fine-grained temporal information and original data distribution attributes from
 137 the Event Cloud, the 2D-spatial and 1D-temporal event information is constructed into a three-
 138 dimensional representation to be processed in Point Cloud. Event Cloud consists of time-series data
 139 capturing spatial intensity changes of images in chronological order, and an individual event is de-
 140 noted as $e_k = (x_k, y_k, t_k, p_k)$, where k is the index representing the k_{th} element in the sequence.
 141 Consequently, the set of events within a single sequence (\mathcal{E}) in the dataset can be expressed as:

$$\mathcal{E} = \{e_k = (x_k, y_k, t_k, p_k) \mid k = 1, \dots, n\} \quad (1)$$

142 For a given pose in the dataset, the ground truth resolution is limited to 5 *ms*, while the event
 143 resolution is 1 μs . Therefore, it is necessary to acquire the events that transpire within the time

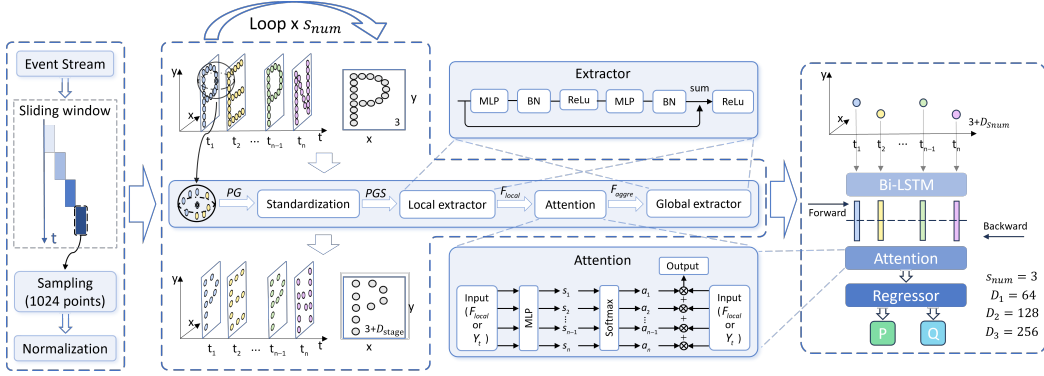


Figure 3: PEPNet overall architecture. The input Event Cloud undergoes direct handling through a sliding window, sampling, and normalization, eliminating the need for any format conversion. Sequentially, the input passes through S_{num} hierarchy structures for spatial feature abstraction and extraction. It further traverses a bidirectional LSTM for temporal feature extraction, culminating in a regressor responsible for 6-DOFs camera pose relocation.

144 period we call it sliding window corresponding to the poses, which will serve as the input for the
 145 model, as depicted by the following equation:

$$\mathcal{P}_i = \{e_{j \rightarrow l} \mid t_l - t_j = R\} \quad i = 1, \dots, M \quad (2)$$

146 The symbol R represents the time interval of the sliding window, where j and l denote the start
 147 and end event index of the sequence, respectively. The variable M represents the number of sliding
 148 windows into which the sequence of events \mathcal{E} is divided. Before being fed into the neural network,
 149 \mathcal{P}_i also needs to undergo sampling and normalization. Sampling is to unify the number of points
 150 N as network inputs. We set $N = 1024$ in PEPNet. Additionally, as the spatial coordinates are
 151 normalized by the camera’s resolution w and h . The normalization process is described by the
 152 following equation:

$$PN_i = \left(\frac{X_i}{w}, \frac{Y_i}{h}, \frac{T_i - t_j}{t_l - t_j} \right) \quad (3)$$

153

$$X_i, Y_i, T_i = \{x_j, \dots, x_l\}, \{y_j, \dots, y_l\}, \{t_j, \dots, t_l\} \quad (4)$$

154 The X, Y is divided by the resolution of the event camera. To normalize T , we subtract the smallest
 155 timestamp t_j of the window and divide it by the time difference $t_l - t_j$, where t_l represents the largest
 156 timestamp within the window. After pre-processing, Event Cloud is converted into the pseudo-Point
 157 Cloud, which comprises explicit spatial information (x, y) and implicit temporal information t .

158 3.2 HIERARCHY STRUCTURE

159 The hierarchy structure is the backbone for processing the pseudo-3D point cloud and is composed
 160 of four primary modules: grouping and sampling, standardization, feature extractor, and aggre-
 161 gation, as described in the following subsection. To efficiently extract deeper explicit spatial and
 162 implicit temporal features, the hierarchical structure is tailored and differs from conventional hier-
 163 archical structure in a few ways: First, we no longer force permutation invariance as usually done
 164 in mainstream point-based methods (Qi et al., 2017a; Ma et al., 2021), as the motion information
 165 is inherently related to the sequential order of events. Instead, we **keep the sequence of all events**
 166 **strictly in the same order** as they are generated to preserve the temporal information to be used
 167 in the next stage. Second, we replace MaxPooling in aggregation and deploy temporal aggregation
 168 which leverages the attention mechanism with softmax, which improves the effective assimilation
 169 of temporal information into the resultant feature vectors.

170 3.2.1 GROUPING AND SAMPLING

171 Aligned with the frame-based design concept, our focus is to capture both local and global infor-
 172 mation. Local information is acquired by leveraging Farthest Point Sampling (FPS) and K-Nearest
 173 Neighbors (KNN), while global information is obtained through a dedicated aggregation module.

$$PS_i = FPS(PN_i) \quad PG_i = KNN(PN_i, PS_i) \quad (5)$$

174 The input dimension PN_i is $[N, 3 + D]$, and the centroid dimension PS_i is $[N', 3 + D]$ and the
 175 group dimension PG_i is $[N', K, 3 + 2 * D]$. K represents the nearest K points of the center point

176 (centroid), D is the feature dimension of the points of the current stage, and 3 is the most original
 177 (X, Y, T) coordinate value. Importantly, it should be noted that the ordering of all points in the
 178 grouping and sampling process strictly adheres to the timestamp (T).

179 3.2.2 STANDARDIZATION

180 Next, each group undergoes a standardization process to ensure consistent variability between points
 181 within the group, as illustrated in this formula:

$$PGS = \frac{PG - PS}{Std(PG)} \quad Std(PG_i) = \sqrt{\frac{\sum_{j=0}^{3n-1} (g_j - \bar{g})^2}{3n - 1}} \quad (6)$$

$$g = [x_0, y_0, t_0, \dots, x_n, y_n, t_n] \quad (7)$$

183 Where PG_i and PS_i are the subsets of PG and PS , Std is the standard deviation, the dimension
 184 of $Std(PG)$ is $[M]$ which is consistent with the number of sliding windows, and g is the set of
 185 coordinates of all points in the PG_i .

186 3.2.3 FEATURE EXTRACTOR

187 Following the standardization of PG by dividing the variance by the subtracted mean, the feature
 188 extraction is performed using a Multi-Layer Perceptron (MLP) with a residual connection. This
 189 process encompasses two steps: local feature extraction and global feature extraction. The feature
 190 extractor with a bottleneck can be mathematically represented as:

$$I(x) = f(BN(MLP_1(x))) \quad (8)$$

$$O(x) = BN(MLP_2(x)) \quad (9)$$

$$Ext(x) = f(x + O(I(x))) \quad (10)$$

193 BN represents batch normalization layer, while f signifies the nonlinear activation function. Both
 194 local feature extraction and global feature extraction maintain identical input and output dimensions.
 195 The dimension increase occurs solely when combining the feature dimension D of the current point
 196 with the feature dimension D of the centroid during grouping, resulting in a final dimension of
 197 $2 * D$. The feature extractor takes an input dimension of $[B, N, K, D]$, and following local feature
 198 extraction, the dimension remains $[B, N, K, D]$, B represents batch size. We adopt the attention
 199 mechanism for aggregation, yielding an aggregated feature dimension of $[B, N, D]$. Subsequently,
 200 the aggregated feature map of $[B, N, D]$ is then processed through the global feature extractor,
 201 completing the feature extraction for the current stage.

202 3.2.4 TEMPORAL AGGREGATION

203 Conventional Point Cloud methods favor MaxPooling operations for feature aggregation because
 204 it is efficient in extracting the feature from one point among a group of points and discarding the
 205 rest. However, MaxPooling involves extracting only the maximum value along each dimension of
 206 the temporal axis. It is robust to noise perturbation but also ignores the temporal nuances embedded
 207 within the features. Conversely, the integration of attention mechanisms enhances the preservation
 208 of those nuanced but useful temporal attributes by aggregating features along the temporal axis
 209 through the attention value. To provide a more comprehensive exposition, we employ a direct at-
 210 tention mechanism within the K temporal dimensions to effectively aggregate features as shown in
 211 Figure 3. This mechanism enables the explicit integration of temporal attributes, capitalizing on the
 212 inherent strict ordering of the K points. The ensuing formula succinctly elucidates the essence of
 213 this attention mechanism:

$$F_{local} = Ext(x) = (S_{t1}, S_{t2}, \dots, S_{tk}) \quad (11)$$

$$A = SoftMax(MLP(F_{local})) = (a_{t1}, a_{t2}, \dots, a_{tk}) \quad (12)$$

$$F_{aggre} = A \cdot F_{local} = S_{t1} \cdot a_{t1} + S_{t2} \cdot a_{t2} + \dots + S_{tk} \cdot a_{tk} \quad (13)$$

216 Upon the application of the local feature extractor, the ensuing features are denoted as F_{local} , and
 217 S_{tk} mean the extracted feature of k_{th} point in a group. The attention mechanism comprises an MLP
 218 layer with an input layer dimension of D and an output a_{tk} dimension of 1, along with softmax
 219 layers. Subsequently, the attention mechanism computes attention values, represented as A . These
 220 attention values are then multiplied with the original features through batch matrix multiplication,
 221 resulting in the aggregated feature F_{aggre} .

222 3.3 A-Bi-LSTM

223 The temporal features extracted through the hierarchical structure are independent and parallel, lack-
 224 ing recurrent mechanisms within the network. This distinctive attribute, referred to as 'implicit',
 225 contrasts with the conventional treatment of temporal information as an indexed process. Conse-
 226 quently, implicit temporal features **inadequately capture the interrelations among events along**
 227 **the timeline**, whereas explicit temporal features assume a pivotal role in facilitating the CPR task.
 228 To explicitly capture temporal patterns, we introduce the LSTM network, which has been proven
 229 effective in learning temporal dependencies. For optimal network performance, controlled feature
 230 dimensionality, and comprehensive capture of bidirectional relationships in pose context, we adopt a
 231 bi-directional LSTM network with a lightweight design. The integration of bidirectional connections
 232 into the recurrent neural network (RNN) is succinctly presented through the following equation:

$$233 \mathbf{h}_t = f(\mathbf{W}_h \cdot \mathbf{x}_t + \mathbf{U}_h \cdot \mathbf{h}_{t-1} + \mathbf{b}_h) \quad (14)$$

$$234 \mathbf{h}'_t = f(\mathbf{W}'_h \cdot \mathbf{x}_t + \mathbf{U}'_h \cdot \mathbf{h}'_{t+1} + \mathbf{b}'_h) \quad (15)$$

$$235 \mathbf{y}_t = \mathbf{V} \cdot \mathbf{h}_t + \mathbf{b}_y \quad (16)$$

$$\mathbf{y}'_t = \mathbf{V}' \cdot \mathbf{h}'_t + \mathbf{b}'_y \quad (17)$$

236 \mathbf{x}_t represents the feature vector at the t -
 237 th time step of the input sequence, while
 238 \mathbf{h}_{t-1} and \mathbf{h}'_{t+1} correspond to the hid-
 239 den states of the forward and backward
 240 RNN units, respectively, from the previ-
 241 ous time step. The matrices \mathbf{W}_h , \mathbf{U}_h ,
 242 and \mathbf{b}_h denote the weight matrix and
 243 bias vector of the forward RNN unit,
 244 while \mathbf{V} and \mathbf{b}_y represent the weight
 245 matrix and bias vector of its output
 246 layer. Similarly, \mathbf{W}'_h , \mathbf{U}'_h , and \mathbf{b}'_h are
 247 associated with the weight matrix and
 248 bias vector of the backward RNN unit,
 249 and \mathbf{V}' and \mathbf{b}'_y pertain to the weight ma-
 250 trix and bias vector of its output layer.
 251 The activation function, denoted as $f(\cdot)$,
 252 can be chosen as sigmoid or tanh or
 253 other functions. The final output Y_a is
 254 aggregated at each moment using the at-
 255 tention mechanism, and \oplus means concat
 256 operation.

$$257 Y_t = y_t \oplus y'_t \quad (18)$$

$$258 A = \text{SoftMax}(MLP(Y_t)) \quad (19)$$

$$Y_a = A \cdot Y_t \quad (20)$$

259 3.4 LOSS FUNCTION

260 A fully connected layer with a hidden
 261 layer is employed to address the final
 262 6-DOFs pose regression task. The dis-
 263 placement vector of the regression is de-
 264 noted as \hat{p} representing the magnitude
 265 and direction of movement, while the rotational Euler angles are denoted as \hat{q} indicating the ro-
 266 tational orientation in three-dimensional space.

$$Loss = \alpha \|\hat{p} - p\|_2 + \beta \|\hat{q} - q\|_2 + \lambda \sum_{i=0}^n w_i^2 \quad (21)$$

267 p and q represent the ground truth obtained from the dataset, while α , β , and λ serve as weight
 268 proportion coefficients. In order to tackle the prominent concern of overfitting, especially in the
 269 end-to-end setting, we propose the incorporation of L2 regularization into the loss function. This
 270 regularization, implemented as the second paradigm for the network weights w , effectively mitigates
 271 the impact of overfitting.

Algorithm 1 PEPNet pipeline

Input: Raw Event Cloud \mathcal{E} **Parameters:** $N_p = 1024, R = 5e + 3, S_{num} = 3$ **Output:** 6-DOFs pose (\hat{p}, \hat{q}) 1: **Preprocessing**2: **for** j **in** $\text{len}(\mathcal{E})$ **do**3: $P_i.append(e_{j \rightarrow l})$; $j = l$; where $t_l - t_j = R$ 4: **if** $(\text{len}(P_i) > N_p)$: $i = i + 1$;5: **end for**6: $PN = \text{Normalize}(\text{Sampling}(P))$

7:

8: **Hierarchy structure**9: **for** stage **in** $\text{range}(S_{num})$ **do**10: **Grouping and Sampling**(PN)11: Get $PGS \in [B, N_{stage}, K, 2 * D_{stage-1}]$ 12: **Local Extractor**(PGS)13: Get $F_{local} \in [B, N_{stage}, K, D_{stage}]$ 14: **Attentive Aggregate**(F_{local})15: Get $F_{aggre} \in [B, N_{stage}, D_{stage}]$ 16: **Global Extractor**(F_{aggre})17: Get $PN = F_{global} \in [B, N_{stage}, D_{stage}]$ 18: **end for**

19:

20: **A-Bi-LSTM**21: Forward Get $y_t \in [B, N_3, D_{S_{num}}/2]$ 22: Reverse Get $y'_t \in [B, N_3, D_{S_{num}}/2]$ 23: Attention Get $Y_a \in [B, D_{S_{num}}]$

24:

25: **Regressor**26: Get 6-DOFs pose (\hat{p}, \hat{q})

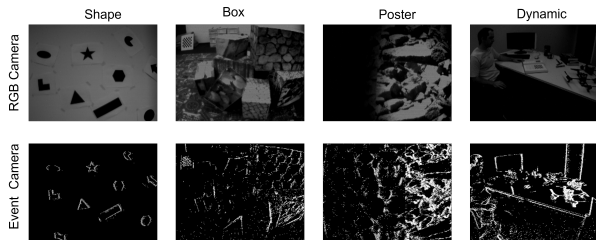


Figure 4: Event-based CPR Dataset visualization.

272 3.5 OVERALL ARCHITECTURE

273 Next, we will present the PEPNet pipeline in pseudo-code, utilizing the previously defined variables
 274 and formulas as described in Algorithm 1.

275 4 EXPERIMENT

276 In this section, we present an extensive and in-depth analysis of PEPNet’s performance on a public
 277 dataset, encompassing evaluations based on rotational and translational mean squared error (MSE),
 278 model parameters, floating-point operations (FLOPs), and inference time. Through a series of sys-
 279 tematic ablation experiments, we experimentally validate the efficacy of each module. PEPNet’s
 280 training and testing are performed on a server furnished with an AMD Ryzen 7950X CPU, an RTX
 281 GeForce 4090 GPU, and 32GB of memory.

282 4.1 DATASET

283 We employ the widely evaluated event-based CPR dataset (Mueggler et al., 2017) collected using
 284 the DAVIS 240C. This dataset encompasses a diverse set of multimodal information, comprising
 285 events, images, IMU measurements, camera calibration, and ground truth information acquired from
 286 a motion capture system operating at an impressive frequency of 200 Hz, thereby ensuring sub-
 287 millimeter precision. We visualized various types of sequences as shown in Figure 4.

288 Two distinct methods to partition the dataset (Nguyen et al., 2019) have been benchmarked: random
 289 split and novel split. In the random split approach, the dataset is randomly selected 70% of all
 290 sequences for training and allocated the remaining sequences for testing. On the other hand, in the
 291 novel split, we divide the data chronologically, using the initial 70% of sequences for training and
 292 the subsequent 30% for testing.

293 4.2 BASELINE

294 We perform a thorough evaluation of our proposed method by comparing it with SOTA event-
 295 based approaches, namely CNN-LSTM (Tabia et al., 2022) and AEARN (Lin et al., 2022). More-
 296 over, we present results derived from other well-established computer vision methods, including
 297 PoseNet(Kendall et al., 2015), Bayesian PoseNet (Kendall & Cipolla, 2016), Pairwise-CNN (Laskar
 298 et al., 2017), LSTM-Pose (Walch et al., 2017), and SP-LSTM(Nguyen et al., 2019).

299 4.3 RANDOM SPLIT RESULTS

300 Based on the findings presented in Table 1, it is apparent that PEPNet surpasses other models con-
 301 cerning both rotation and translation errors across all sequences. Notably, PEPNet achieves these
 302 impressive results despite utilizing significantly fewer model parameters and FLOPs compared to
 303 the frame-based approach. Moreover, PEPNet not only exhibits a remarkable 38% improvement in
 304 the average error compared to the SOTA CNN-LSTM method but also attains superior results across
 305 nearly all sequences. In addressing the more intricate and challenging `hdr_poster` sequences, while
 306 the frame-based approach relies on a denoising network to yield improved results (Jin et al., 2021),
 307 PEPNet excels by achieving remarkable performance without any additional processing. This ob-
 308 servation strongly implies that PEPNet’s point cloud approach exhibits greater robustness compared
 309 to the frame-based method, highlighting its inherent superiority in handling complex scenarios.

310 Furthermore, we introduce an alternative variant, PEPNet_{tiny}, which integrates a lighter model ar-
 311 chitecture while preserving relatively strong performance. As depicted in Figure 3, PEPNet consists

Network	PoseNet	Bayesian PoseNet	Pairwise-CNN	LSTM-Pose	SP-LSTM	CNN-LSTM	PEPNet	PEPNet _{tiny}
Parameter	12.43M	22.35M	22.34M	16.05M	135.25M	12.63M	<u>0.774M</u>	0.064M
FLOPs	1.584G	3.679G	7.359G	1.822G	15.623G	1.960G	<u>0.459G</u>	0.033G
shapes_rotation	0.109m,7.388°	0.142m,9.557°	0.095m,6.332°	0.032m,4.439°	0.025m,2.256°	0.012m,1.652°	0.005m,1.372°	0.006m,1.592°
box_translation	0.193m,6.977°	0.190m,6.636°	0.178m,6.153°	0.083m,6.215°	0.036m,2.195°	0.013m,0.873°	<u>0.017m,0.845°</u>	0.031m,1.516°
shapes_translation	0.238m,6.001°	0.264m,6.235°	0.201m,5.146°	0.056m,5.018°	0.035m,2.117°	0.020m,1.471°	0.011m,0.582°	<u>0.013m,0.769°</u>
dynamic_6dof	0.297m,9.332°	0.296m,8.963°	0.245m,5.962°	0.097m,6.732°	0.031m,2.047°	<u>0.016m,1.662°</u>	0.015m,1.045°	0.018m,1.144°
hdr_poster	0.282m,8.513°	0.290m,8.710°	0.232m,7.234°	0.108m,6.186°	0.051m,3.354°	0.033m,2.421°	0.016m,0.991°	<u>0.028m,1.863°</u>
poster_translation	0.266m,6.516°	0.264m,5.459°	0.211m,6.439°	0.079m,5.734°	0.036m,2.074°	0.020m,1.468°	0.012m,0.588°	0.019m,0.953°
Average	0.231m,7.455°	0.241m,7.593°	0.194m,6.211°	0.076m,5.721°	0.036m,2.341°	0.019m,1.591°	0.013m,0.904°	0.019m,1.306°

Table 1: Random split results. The table presents the median error for each sequence, as well as the average error across the six sequences. It also presents the number of parameters and FLOPs for each model. Bold indicates the most advanced result, while underline signifies the second-best result.

Network	PoseNet	Bayesian PoseNet	Pairwise-CNN	LSTM-Pose	SP-LSTM	DSAC*	AECRN	PEPNet
shapes_rotation	0.201m,12.499°	0.164m,12.188°	0.187m,10.426°	0.061m,7.625°	0.045m,5.017°	0.029m,2.3°	<u>0.025m,2.0°</u>	0.016m,1.745°
shapes_translation	0.198m,6.696°	0.213m,7.441°	0.225m,11.627°	0.108m,8.468°	0.072m,4.496°	0.038m,2.2°	<u>0.029m,1.7°</u>	0.026m,1.659°
shapes_6dof	0.320m,13.733°	0.326m,13.296°	0.314m,13.245°	0.096m,8.973°	0.078m,5.524°	0.054m,3.1°	<u>0.052m,3.0°</u>	0.045m,2.984°
Average	0.240m,11.067°	0.234m,10.975°	0.242m,11.766°	0.088m,8.355°	0.065m,5.012°	0.040m,2.53°	<u>0.035m,2.23°</u>	0.029m,2.13°
Inference time	5ms	6ms	12ms	9.49ms	4.79ms	30ms	30ms	6.7ms

Table 2: Novel split results. Referred to as Table I, showcases identical information. To assess the model’s runtime, we conduct tests on a server platform, specifically focusing on the average time required for inference on a single sample.

of three stages, and the model’s size is contingent upon the dimensionality of MLPs at each stage. The dimensions for the standard structure are [64, 128, 256], whereas those for the tiny structure are [16, 32, 64]. As indicated in Table 1, even with a mere 0.5% of the CNN-LSTM’s parameter, PEPNet_{tiny} achieves comparable and even slightly superior results. This remarkable outcome emphasizes the superiority of leveraging event cloud data processing directly.

Although PEPNet_{tiny} demonstrates the potential to outperform previous SOTA results in terms of the final average performance, it reveals evident weaknesses and underfitting when handling more complex sequences, such as `hdr_poster` and `box_translation`. The limitations in the abstraction ability of PEPNet_{tiny} become apparent. It is important to acknowledge that PEPNet’s results might improve with a larger dataset, indicating the significant impact of data size on the model’s performance.

4.4 ERROR DISTRIBUTION

Figure 5 illustrates the error distribution of PEPNet across six distinct sequences using the random split method, specifically: shape rotation, box translation, shape translation, dynamic 6-dof, `hdr_poster`, and `poster_translation`. To enhance clarity, the top and bottom boundaries of the box represent the first and third quartiles, respectively, indicating the inter-quartile range (IQR). The median is denoted by the band within the box. It is observed that the IQR of the translation error approximately locates between 0.004m and 0.024m, while the orientation error ranges from 0.4° to 1.9°.

Among the six sequences, shape rotation and box translation display the poorest results in rotation and translation, respectively, primarily due to the inherent complexity of the dataset. As the scene becomes more intricate and the resolution increases, such as in the `hdr_poster`, the model is challenged to exhibit its robustness. Notably, PEPNet demonstrates enhancements of approximately 50% compared to the SOTA model in this scenario.

4.5 NOVEL SPLIT RESULTS

To assess the model’s robustness, we adopt the novel split as an evaluation criterion, as shown in Table 2. During the training process, we observe a more pronounced overfitting phenomenon in PEPNet compared to the random split. We attribute this observation to the disparities in data distributions between the trainset and the testset, as well as the limited data size. Contrary to the

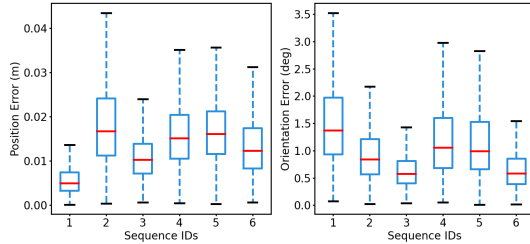


Figure 5: Error distribution of event-based CPR results achieved by PEPNet using a random split. (a) Translation errors. (b) Rotation errors.

Condition	HS	LSTM	Bi-LSTM	Aggregation	Translation	Rotation	T+R
1	✓			Max	0.015m	0.884°	3.04
2	✓			Temporal	0.014m	0.786°	2.77
3	✓	✓		Max	0.014m	0.833°	2.85
4	✓		✓	Max	0.014m	0.813°	2.82
5	✓		✓	Temporal	0.011m	0.582°	2.12

Table 3: Ablation Study for three key modules. T+R = Translation + Rotation· $\pi/180$ (m+rad)

346 methods we compared, PEPNet does not necessitate pre-trained weights. For instance, SP-LSTM
 347 relies on pre-trained VGG19 weights from Imagenet, while AEARN requires synthetic heuristic
 348 depth and an extensive pretraining process.

349 To address overfitting, PEPNet employs conventional methods that yield consistent and comparable
 350 results with the SOTA on three shape sequences that are displayed in the network column of Table 2.
 351 It is essential to note that AEARN adopts a hybrid approach, combining neural network regression
 352 for scene coordinates with derivable RANSAC for pose estimation. Moreover, this method incurs
 353 significant time consumption, with even the SOTA DSAC* algorithm taking nearly 30ms, excluding
 354 additional time for format conversion. This time constraint presents compatibility challenges with
 355 the low-latency nature of event cameras. In contrast, PEPNet can execute on a server in just 6.7ms,
 356 with the main time-consuming module being grouping and sampling. Furthermore, with potential
 357 field programmable gate array (FPGA) or application-specific integrated chip (ASIC) support for
 358 these operations, PEPNet’s performance can be further accelerated.

359 4.6 ATTENTION VISUALIZATION

360 As shown in Figure 6, We observe that the values exhibit larger at both the start and end. Our con-
 361 jecture posits that during the process of camera pose relocalization, the model may intensify its empha-
 362 sis on the distinctions in features between the initial and terminal points, and regress the 6DOFs pose
 363 through the differences, similar to geometric methods Mueggler et al. (2018); Gallego et al. (2015).
 364

365 4.7 ABLATION STUDY

366 In order to validate the efficacy of key modules,
 367 we conducted ablation experiments focusing on
 368 three primary components: hierarchy structure,
 369 Bi-LSTM, and attention. These experiments
 370 are designed to evaluate rotation and transla-
 371 tion errors on the shape translation sequence
 372 with random split. The combined error (T+R)
 373 is measured after processing.

374 Our experimental setup comprises four distinct
 375 conditions, as illustrated in Table 3. Condition
 376 1 represents the sole utilization of the hierarchy
 377 structure (HS), while Condition 2 combines the ordinary LSTM. Condition 3 incorporates the bidi-
 378 rectional LSTM, and Condition 4 integrates the attention mechanism for feature aggregation.

379 The ablation experiments reveal significant insights. Experiments 1 and 2 demonstrate that aug-
 380 menting LSTM enhances the extraction of explicit temporal features. Moreover, experiments 2 and
 381 3 reveal the effectiveness of the bidirectional LSTM in extracting motion information. Additionally,
 382 experiments 3 and 4 confirm the notable impact of attention in feature aggregation, resulting in a
 383 substantial reduction in error rates.

384 5 CONCLUSION

385 In this paper, we introduce an end-to-end CPR network that operates directly on raw event clouds
 386 without frame-based preprocessing. PEPNet boasts an impressively lightweight framework that
 387 adeptly extracts spatial and temporal features, leading to SOTA outcomes on publicly accessible
 388 datasets. Diverging from traditional frame-based approaches, our method prioritizes preserving
 389 the inherent distribution of the event camera output, capitalizing on its sparse nature to achieve
 390 extraordinary capabilities for ultra-low-power CPR applications.

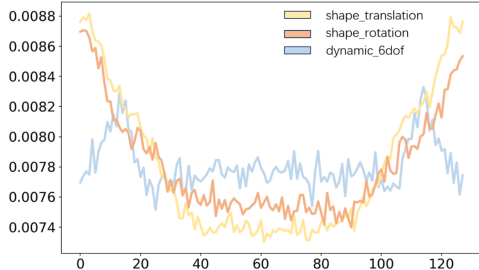


Figure 6: Visualization of the attention values in the time domain. 128 points in chronological order on the horizontal axis and the attention values of the corresponding point on the vertical axis.

391 REFERENCES

- 392 Vassileios Balntas, Shuda Li, and Victor Prisacariu. Relocnet: Continuous metric learning re-
393 calisation using neural nets. In *Proceedings of the European Conference on Computer Vision*
394 (*ECCV*), pp. 751–767, 2018.
- 395 Eric Brachmann and Carsten Rother. Visual camera re-localization from rgb and rgb-d images using
396 dsac. *IEEE transactions on pattern analysis and machine intelligence*, 44(9):5847–5865, 2021.
- 397 Eric Brachmann, Alexander Krull, Sebastian Nowozin, Jamie Shotton, Frank Michel, Stefan
398 Gumhold, and Carsten Rother. Dsac-differentiable ransac for camera localization. In *Proceedings*
399 *of the IEEE conference on computer vision and pattern recognition*, pp. 6684–6692, 2017.
- 400 Tobi Delbruck and Manuel Lang. Robotic goalie with 3 ms reaction time at 4% cpu load using
401 event-based dynamic vision sensor. *Frontiers in neuroscience*, 7:223, 2013.
- 402 Alexey Dosovitskiy, Lucas Beyer, Alexander Kolesnikov, Dirk Weissenborn, Xiaohua Zhai, Thomas
403 Unterthiner, Mostafa Dehghani, Matthias Minderer, Georg Heigold, Sylvain Gelly, et al. An im-
404 age is worth 16x16 words: Transformers for image recognition at scale. In *International Confer-*
405 *ence on Learning Representations*, 2020.
- 406 Guillermo Gallego, Christian Forster, Elias Mueggler, and Davide Scaramuzza. Event-based camera
407 pose tracking using a generative event model. *arXiv preprint arXiv:1510.01972*, 2015.
- 408 Guillermo Gallego, Jon EA Lund, Elias Mueggler, Henri Rebecq, Tobi Delbruck, and Davide Scara-
409 muzza. Event-based, 6-dof camera tracking from photometric depth maps. *IEEE transactions on*
410 *pattern analysis and machine intelligence*, 40(10):2402–2412, 2017.
- 411 Guillermo Gallego, Tobi Delbrück, Garrick Orchard, Chiara Bartolozzi, Brian Taba, Andrea Censi,
412 Stefan Leutenegger, Andrew J Davison, Jörg Conradt, Kostas Daniilidis, et al. Event-based vision:
413 A survey. *IEEE transactions on pattern analysis and machine intelligence*, 44(1):154–180, 2020.
- 414 Yulan Guo, Hanyun Wang, Qingyong Hu, Hao Liu, Li Liu, and Mohammed Bannamoun. Deep
415 learning for 3d point clouds: A survey. *IEEE transactions on pattern analysis and machine*
416 *intelligence*, 43(12):4338–4364, 2020.
- 417 Kaiming He, Xiangyu Zhang, Shaoqing Ren, and Jian Sun. Deep residual learning for image recog-
418 nition. In *Proceedings of the IEEE conference on computer vision and pattern recognition*, pp.
419 770–778, 2016.
- 420 Yifan Jin, Lei Yu, Guangqiang Li, and Shumin Fei. A 6-dofs event-based camera relocalization
421 system by cnn-lstm and image denoising. *Expert Systems with Applications*, 170:114535, 2021.
- 422 Alex Kendall and Roberto Cipolla. Modelling uncertainty in deep learning for camera relocalization.
423 In *2016 IEEE international conference on Robotics and Automation (ICRA)*, pp. 4762–4769.
424 IEEE, 2016.
- 425 Alex Kendall, Matthew Grimes, and Roberto Cipolla. Posenet: A convolutional network for real-
426 time 6-dof camera relocalization. In *Proceedings of the IEEE international conference on com-*
427 *puter vision*, pp. 2938–2946, 2015.
- 428 Zakaria Laskar, Iaroslav Melekhov, Surya Kalia, and Juho Kannala. Camera relocalization by com-
429 puting pairwise relative poses using convolutional neural network. In *Proceedings of the IEEE*
430 *International Conference on Computer Vision Workshops*, pp. 929–938, 2017.
- 431 Yann LeCun, Yoshua Bengio, and Geoffrey Hinton. Deep learning. *nature*, 521(7553):436–444,
432 2015.
- 433 Patrick Lichtsteiner, Christoph Posch, and Tobi Delbruck. A 128×128 120 db 15 μ s latency
434 asynchronous temporal contrast vision sensor. *IEEE journal of solid-state circuits*, 43(2):566–
435 576, 2008.

- 436 Hu Lin, Meng Li, Qianchen Xia, Yifeng Fei, Baocai Yin, and Xin Yang. 6-dof pose relocation
437 for event cameras with entropy frame and attention networks. In *The 18th ACM SIGGRAPH*
438 *International Conference on Virtual-Reality Continuum and its Applications in Industry*, pp. 1–8,
439 2022.
- 440 Yimin Lin, Zhaoxiang Liu, Jianfeng Huang, Chaopeng Wang, Guoguang Du, Jinqiang Bai, and
441 Shiguo Lian. Deep global-relative networks for end-to-end 6-dof visual localization and odome-
442 try. In *PRICAI 2019: Trends in Artificial Intelligence: 16th Pacific Rim International Conference*
443 *on Artificial Intelligence, Cuvu, Yanuca Island, Fiji, August 26–30, 2019, Proceedings, Part II*,
444 pp. 454–467. Springer, 2019.
- 445 Xu Ma, Can Qin, Haoxuan You, Haoxi Ran, and Yun Fu. Rethinking network design and local
446 geometry in point cloud: A simple residual mlp framework. In *International Conference on*
447 *Learning Representations*, 2021.
- 448 Anton Mitrokhin, Chengxi Ye, Cornelia Fermüller, Yiannis Aloimonos, and Tobi Delbruck. Ev-
449 imo: Motion segmentation dataset and learning pipeline for event cameras. In *2019 IEEE/RSJ*
450 *International Conference on Intelligent Robots and Systems (IROS)*, pp. 6105–6112. IEEE, 2019.
- 451 Anton Mitrokhin, Zhiyuan Hua, Cornelia Fermuller, and Yiannis Aloimonos. Learning visual mo-
452 tion segmentation using event surfaces. In *Proceedings of the IEEE/CVF Conference on Computer*
453 *Vision and Pattern Recognition*, pp. 14414–14423, 2020.
- 454 Elias Mueggler, Henri Rebecq, Guillermo Gallego, Tobi Delbruck, and Davide Scaramuzza. The
455 event-camera dataset and simulator: Event-based data for pose estimation, visual odometry, and
456 slam. *The International Journal of Robotics Research*, 36(2):142–149, 2017.
- 457 Elias Mueggler, Guillermo Gallego, Henri Rebecq, and Davide Scaramuzza. Continuous-time
458 visual-inertial odometry for event cameras. *IEEE Transactions on Robotics*, 34(6):1425–1440,
459 2018.
- 460 Tayyab Naseer and Wolfram Burgard. Deep regression for monocular camera-based 6-dof global
461 localization in outdoor environments. In *2017 IEEE/RSJ International Conference on Intelligent*
462 *Robots and Systems (IROS)*, pp. 1525–1530. IEEE, 2017.
- 463 Anh Nguyen, Thanh-Toan Do, Darwin G Caldwell, and Nikos G Tsagarakis. Real-time 6dof
464 pose relocation for event cameras with stacked spatial lstm networks. In *Proceedings of the*
465 *IEEE/CVF Conference on Computer Vision and Pattern Recognition Workshops*, pp. 0–0, 2019.
- 466 Christoph Posch, Daniel Matolin, and Rainer Wohlgenannt. A qvga 143 db dynamic range frame-
467 free pwm image sensor with lossless pixel-level video compression and time-domain cds. *IEEE*
468 *Journal of Solid-State Circuits*, 46(1):259–275, 2010.
- 469 Charles R Qi, Hao Su, Kaichun Mo, and Leonidas J Guibas. Pointnet: Deep learning on point sets
470 for 3d classification and segmentation. In *Proceedings of the IEEE conference on computer vision*
471 *and pattern recognition*, pp. 652–660, 2017a.
- 472 Charles Ruizhongtai Qi, Li Yi, Hao Su, and Leonidas J Guibas. Pointnet++: Deep hierarchical fea-
473 ture learning on point sets in a metric space. *Advances in neural information processing systems*,
474 30, 2017b.
- 475 Noha Radwan, Abhinav Valada, and Wolfram Burgard. Vlocnet++: Deep multitask learning for
476 semantic visual localization and odometry. *IEEE Robotics and Automation Letters*, 3(4):4407–
477 4414, 2018.
- 478 Henri Rebecq, Daniel Gehrig, and Davide Scaramuzza. Esim: an open event camera simulator. In
479 *Conference on robot learning*, pp. 969–982. PMLR, 2018.
- 480 Hongwei Ren, Yue Zhou, Haotian Fu, Yulong Huang, Renjing Xu, and Bojun Cheng. Tpoint:
481 A tensorized point cloud network for lightweight action recognition with event cameras. *arXiv*
482 *preprint arXiv:2308.09993*, 2023.
- 483 Yoli Shavit and Ron Ferens. Introduction to camera pose estimation with deep learning. *arXiv*
484 *preprint arXiv:1907.05272*, 2019.

- 485 Karen Simonyan and Andrew Zisserman. Very deep convolutional networks for large-scale image
486 recognition. *arXiv preprint arXiv:1409.1556*, 2014.
- 487 Niko Sünderhauf, Sareh Shirazi, Feras Dayoub, Ben Upcroft, and Michael Milford. On the perfor-
488 mance of convnet features for place recognition. In *2015 IEEE/RSJ international conference on*
489 *intelligent robots and systems (IROS)*, pp. 4297–4304. IEEE, 2015.
- 490 Ahmed Tabia, Fabien Bonardi, and Samia Bouchafa. Deep learning for pose estimation from event
491 camera. In *2022 International Conference on Digital Image Computing: Techniques and Appli-*
492 *cations (DICTA)*, pp. 1–7. IEEE, 2022.
- 493 Abhinav Valada, Noha Radwan, and Wolfram Burgard. Deep auxiliary learning for visual localiza-
494 tion and odometry. In *2018 IEEE international conference on robotics and automation (ICRA)*,
495 pp. 6939–6946. IEEE, 2018.
- 496 Florian Walch, Caner Hazirbas, Laura Leal-Taixe, Torsten Sattler, Sebastian Hilsenbeck, and Daniel
497 Cremers. Image-based localization using lstms for structured feature correlation. In *Proceedings*
498 *of the IEEE International Conference on Computer Vision*, pp. 627–637, 2017.
- 499 Qinyi Wang, Yexin Zhang, Junsong Yuan, and Yilong Lu. Space-time event clouds for gesture recog-
500 nition: From rgb cameras to event cameras. In *2019 IEEE Winter Conference on Applications of*
501 *Computer Vision (WACV)*, pp. 1826–1835. IEEE, 2019.
- 502 Jian Wu, Liwei Ma, and Xiaolin Hu. Delving deeper into convolutional neural networks for camera
503 relocalization. In *2017 IEEE International Conference on Robotics and Automation (ICRA)*, pp.
504 5644–5651. IEEE, 2017.
- 505 Wenxuan Wu, Zhongang Qi, and Li Fuxin. Pointconv: Deep convolutional networks on 3d point
506 clouds. In *Proceedings of the IEEE/CVF Conference on Computer Vision and Pattern Recogni-*
507 *tion*, pp. 9621–9630, 2019.
- 508 Jiancheng Yang, Qiang Zhang, Bingbing Ni, Linguo Li, Jinxian Liu, Mengdie Zhou, and Qi Tian.
509 Modeling point clouds with self-attention and gumbel subset sampling. In *Proceedings of the*
510 *IEEE/CVF conference on computer vision and pattern recognition*, pp. 3323–3332, 2019.
- 511 Hengshuang Zhao, Li Jiang, Jiaya Jia, Philip HS Torr, and Vladlen Koltun. Point transformer. In
512 *Proceedings of the IEEE/CVF International Conference on Computer Vision*, pp. 16259–16268,
513 2021.